The Cryosphere
Discussions

Water tracks intensify surface energy and mass exchange in the Antarctic McMurdo Dry Valleys

Tobias Linhardt[1], Joseph S. Levy[2], and Christoph K. Thomas[1,3]

[1]Micrometeorology Group, University of Bayreuth, Bayreuth, Bavaria, Germany
[2]Department of Geology, Colgate University, Hamilton, New York, USA
[3]Bayreuth Center of Ecology and Environmental Research (BayCEER), University of Bayreuth, Bayreuth, Bavaria, Germany

Correspondence: Tobias Linhardt (tobias.linhardt@uni-bayreuth.de)

Abstract. We evaluated the hypotheses that water tracks alter the surface energy balance in the Antarctic McMurdo Dry Valleys and may serve as an indicator of landscape response to climate change in this dry, cold and ice-sheet-free environment. Water tracks are channel-shaped high moisture zones in the active layer of polar soils. The surface energy balance was measured for one water-track and two non-water-track reference locations in Taylor Valley during the Antarctic summer of 2012–2013.

5 Turbulent atmospheric fluxes of sensible heat and evaporation were observed using the eddy-covariance method in combination with flux footprint modeling, which was the first application of this state-of-the-art technique in the Dry Valleys. Soil heat fluxes were analyzed separately for thawed and frozen layers at all locations via computing the change of the heat storage in the thawed layer from measurements.

The results showed that for both water track and reference locations over 50 % of the net radiation was transferred to sensible

10 heat exchange, about 30 % to melting the seasonally thawed layer, and the remainder to evaporation. The net energy flux in the thawed layer was zero. For the water track location, evaporation was increased by a factor of 3.0 relative to the references, ground heat fluxes by 1.4, and net radiation by 1.1, while sensible heat fluxes were reduced down to 0.7. Entertaining a realistic scenario of climate change in Taylor Valley in which the land cover fraction of water tracks increases by 50 %, the total evaporation from lower Taylor Valley would increase by 4 % to 0.30 mm d^{-1}.

15 In summary, our findings show that water tracks have a strong impact on the surface energy balance in ice-sheet free Antarctic regions. Water tracks are hot spots of change and are likely to respond faster to climate change signals than the dominant dry glacial till in the McMurdo Dry Valleys. Their spatiotemporal dynamics may therefore serve as indicator of high-sensitivity for change in permafrost-dominated cold landscapes.

1 Introduction

20 The McMurdo Dry Valleys (MDV) are an ice-sheet free area in continental Antarctica characterized by bare permafrost-affected soils, glaciers, ice-covered lakes and ephemeral streams (Lyons et al., 2000). Despite their geographical remoteness, the MDV are subject to a changing climate showing opposite trends in sign of varying magnitude over the past decades. From 1986 to 2002 the MDV experienced a cooling trend of 0.7 K per decade (Doran et al., 2002b). The cooling stopped around 2002, when high temperatures and increasing insolation caused strong glacial melt which led to several well-documented ecosystem

changes including lake-level rise and increased biological production. The period post 2002 has shown no trends in temperature (Gooseff et al., 2017). A distinct increase in Thermokarst formation in the MDV indicates ongoing landscape change caused by thawing processes (Levy, 2013). For the near future, a rise in temperature and a likely precipitation increase is predicted throughout Antarctica (Christensen et al., 2014). Empirical evidence for this new trend is provided by an accelerating decrease

5   of the Antarctic ice sheet volume (Pachauri and Mayer, 2015).

In addition to the above-mentioned well-studied indicators for Antarctic climate change, the spatiotemporal dynamics of water tracks may serve as yet another indicator for change in the MDV. Water tracks are channel-shaped high moisture and zones of high salinity in the active layer of polar soils generating shallow groundwater flow (Levy et al., 2011). This indicator is potentially even more sensitive since water tracks are small-scale, scattered features in the MDV landscape occupying a

10   small fraction of the total area, but with stark contrasting surface radiative, thermal, and soil properties. Compared to their surroundings, water tracks feature an increased soil water content and elevated solute concentrations (Levy et al., 2011; Ball and Levy, 2015), and a thicker active layer than the surrounding soil owing to an increased thermal conductivity and reduced albedo (Levy and Schmidt, 2016; Levy et al., 2011; Ikard et al., 2009).

Since the characteristics of water tracks depend on the rate of the energy and mass exchange with the surrounding non-water

15   track MDV soils and near-surface air, variations in climate elements including insolation, air temperature, precipitation and evaporative demand are important drivers. It is likely that properties and abundance of water tracks in the MDV will respond to the ongoing climate change. Here, we identify an opportunity to investigate the utility of this potentially useful indicator of climate change in the MDV.

The objective of our study is to quantify the impact of water tracks on vertical energy and water exchange in MDV cold

20   desert soils. Given the lower albedo and higher soil water content of water tracks, we hypothesize that the energy uptake of water-track surfaces is enhanced compared to the adjacent, dry, off-water track soils. Logically, we hypothesize that latent heat flux and ground heat flux are increased on water-track surfaces compared to their surrounding. Based on this increase rate of energy and mass exchange, water tracks may be the most sensitive zones responding to climate change in the MDV and therefore serve as an indicator of change in this landscape.

25   2   Constructing a conceptual surface energy budget

We define the surface energy balance (SEB) as the equilibrium between net radiation Q_S^* at the surface and the sum of sensible heat flux Q_H, latent heat flux Q_{LE} and ground heat flux Q_G:

$$-Q_S^* = Q_H + Q_{LE} + Q_G. \tag{1}$$

The change of heat storage at the surface was neglected, as no vegetation or built infrastructure is present in this environment.

30   The magnitude of the ground heat flux in a cold-desert energy budget can be substantial because thawing of the ice table requires a large amount of energy (Lloyd et al., 2001). We decided to divide the ground heat flux Q_G into the temporal change in heat storage in the thawed layer ΔS_{TL} and into the soil heat flux Q_{IT} at ice table depth which is dominated by the ice table
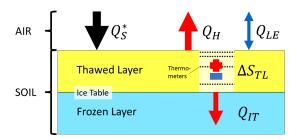
Figure 1. Surface energy balance concept used in this study, with net radiation Q_S^*, sensible heat flux Q_H, latent heat flux Q_{LE}, temporal storage change in the thawed layer ΔS_{TL} and soil heat flux at ice table depth Q_{IT}. Ground heat flux is given by adding together ΔS_{TL} and Q_{IT}. Arrows depict observed directions of energy fluxes.

melting energy (Fig. 1):

$$Q_G = \Delta S_{TL} + Q_{IT}, \tag{2}$$

where ΔS_{TL} equals the temporal heat storage change between surface and ice table depth $-z_{IT}(t)$ and was determined using a calorimetric approach following Liebethal and Foken (2007):

$$\Delta S_{TL} = \int_{-z_{IT}(t)}^{0} \frac{\delta}{\delta t} C_G(-z) T(-z)\, dz. \tag{3}$$

The thickness of the thawed layer was assumed to be constant throughout the measuring period, though in reality it likely changed over time due to lowering of the ice table as a result of continued melting. The impact of this assumption on the surface energy balance is discussed in Appendix A.

The turbulent sensible heat flux and latent heat flux, i.e., evaporation, were computed using the eddy-covariance (EC) method in combination with flux footprint modeling. The micrometeorological EC method is the state-of-the-art tool for quantifying turbulent energy and mass net exchange between the land surface and the atmosphere with high precision, and is used at more than 700 sites globally across all climate zones and biomes (e.g. Baldocchi, 2003; Aubinet et al., 2000). It is based upon turbulence observations and the application of the Reynolds decomposition ($X = \overline{X} + X'$), which divides a scalar or vector quantity X into its temporal mean $\overline{X}$ and temporal perturbation X' to compute the net flux. According to Reynolds' second postulate, the total vertical net flux $\overline{wX}$, which is computed from the measurements of the vertical wind speed w and quantity X, in the surface layer becomes $\overline{wX} = \overline{w'X'}$ under the assumption that $\overline{w} = 0$ ms^{-1} for continuity reasons. Thus, Q_H and Q_{LE} in energetic units (Wm^{-2}) were calculated using Eq. (4) and Eq. (5) from the covariances of w and air temperature $X = T$ ($\overline{w'T'}$, m K s^{-1}) and specific humidity $X = q$ ($\overline{w'q'}$, kg kg^{-1} m s^{-1}), respectively:

$$Q_H = c_p \rho \overline{w'T'} \tag{4}$$

$$Q_{LE} = \rho\lambda\overline{w'q'}, \tag{5}$$

where c_p ($\mathrm{J\,K^{-1}\,kg^{-1}}$) is the specific heat capacity of air, ρ ($\mathrm{kg\,m^{-3}}$) is the air density, and λ ($\mathrm{J\,kg^{-1}}$) is the latent heat
of vaporization. Flux footprint modeling was used to distinguish between turbulent fluxes originating from water tracks and
5   those from non-water track surfaces. Our intention was to isolate the effect of these small-scale features, which may occupy
only several tens to hundreds of square meters, onto the SEB. Flux footprint modeling is the state-of-the-art tool which allows
for connecting the recorded turbulence signals at sensor location to their source area (see e.g. Leclerc and Foken, 2014, and
references therein). Based upon well-known laws for isotropic and homogeneous turbulent airflows, flux footprint models
compute a spatially explicit probability density function, i.e., the flux footprint, quantifying the contribution of each grid cell of
10 the land use-matrix to the total observed flux (see Fig. 3). Since these contributions and thus the source area varies with sensor
height, surface properties, and airflow properties including turbulence statistics, wind speed, and wind direction, one may select
intervals for which the turbulent flux predominantly originates from a certain land cover-type of interest. The complete SEB
equation applied in this study then equates to

$$-Q_S^* = c_p\rho\overline{w'T'} + \rho\lambda\overline{w'q'} + \int\limits_{-z_{IT}(t)}^{0} \frac{\delta}{\delta t}C_G(-z)T(-z)\,dz + Q_{IT}, \tag{6}$$

15 where $C_G(-z)$ ($\mathrm{J\,m^{-3}\,K^{-1}}$) is the volumetric heat capacity of the soil.

3   Field observations

Measurements were taken over 26 days during the Antarctic summer 2012/ 2013 at three closely collocated sites near the
shore in lower Taylor Valley, MDV. At any time during the experiment, two EC and SEB stations were operated: Throughout
the whole period one station was installed at a water track. The other station was successively operated as a reference at two
20 different locations with surfaces representing the main non-water track, bare soil surfaces in lower Taylor Valley. Reference 1
was located on a paleolake delta dominated by fine sediments, while Reference 2 represents coarse glacial till (Fig. 2).

Each station consisted of a net radiometer (*NR01, Hukseflux Thermal Sensors B.V., Delft, NL*) for measuring incoming
and outgoing longwave and shortwave radiation components, an ultrasonic anemometer (*81000 VRE, R.M. Young Company,
Traverse City, MI, USA*) and an infrared gas analyzer (*LI-7500, LI-COR Inc., Lincoln, NE, USA*), both for eddy-covariance
25 measurements. Soil temperatures were recorded in different depths with thermistors and thermocouples (Table C1). Sonic
anemometer measurements providing wind and acoustic temperature data and infrared gas analyzer measurements of water
vapor and carbon dioxide concentrations were sampled and recorded at 20 Hz.

For the computation of ΔS_{TL}, temperature profiles of the thawed layer with logarithmic interpolations between temperature
measurements in several depths were used. Ice table depths were determined by depth-to-refusal measurements to 0.48 m for
30 the water track and 0.30 m for Reference 1. For the water track the temperature at the ice table was assumed to be 0 °C. At
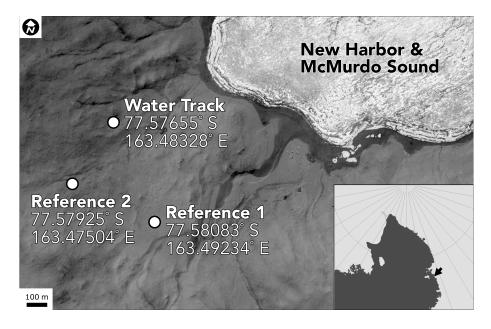
Figure 2. Study site in lower Taylor Vallley with the locations of the three sites near Ross Ice Shelf. The image is an excerpt from Worldview-1 image WV01-20151218225356-1020010047AA1800, collected 18 December 2015, and is overlain on a hillshade of the LiDAR dataset from Fountain et al. (2017). Inset map shows location of the Taylor Valley study site on the Ross Sea and is gridded by 10° latitude/ longitude lines.

Reference 1 ground temperature was measured at ice table depth. The mean temperature of 1.9 °C recorded by this deepest thermometer was used for the ice table depth when direct temperature measurements were unavailable and for Reference 2. For the calculation of ΔS_{TL}, we measured volumetric heat capacity of the soil in-situ.

4   Data processing

Eddy-Covariance fluxes were computed using a fixed perturbation time scale of 30 minutes using the bmmflux tool software of the Micrometeorology Group of the University of Bayreuth (see appendix in Thomas et al., 2009). First the raw data were filtered by instrument flags and plausibility limits. A despiking routine was applied to exclude unphysical turbulence data (Vickers and Mahrt, 1997). Time lags between gas analyzer and anemometer were corrected by maximizing the covariances of the measured quantities. A 3-dimensional rotation routine was used to rotate into the mean streamlines and eliminate the mean vertical wind (Wilczak et al., 2001). Computed fluxes were spectrally correction following Moore (1986). The buoyancy flux was converted into sensible heat flux by a post-hoc buoyancy correction (Schotanus et al., 1983). A post-hoc density correction was applied to the latent heat and carbon dioxide fluxes (Webb et al., 1980). EC quality flags for turbulent fluxes following Foken et al. (2004) were used to filter for intervals with flags ≤ 1 in which the assumption of stationarity and well-developed turbulence were satisfied.

ΔS_{TL} was determined as temporal heat storage change via calorimetry with Eq. (3). A sensitivity analysis showed that differences in ΔS_{TL} between water-track and reference stations were larger than errors induced by a possible miscalculation of z_{IT} (Appendix A). The second component of the ground heat flux – Q_{IT} – was approximated as the remaining SEB residual after adding together Q_S^*, Q_H, Q_{LE} and ΔS_{TL}. The computed ΔS_{TL} was discarded when calculated from temperature measurements at one depth only, which applied to 34 % for the water track. The resulting data gaps resulted in 2-6 % of available data for most SEB components. The gaps were filled by linear interpolation whenever possible. The surface energy balance was only evaluated for intervals when all its components were available.

The time-variant footprint of the turbulent energy and mass fluxes for the water-track station was modeled with the Lagrangian-statistics backward TERRAFEX model of the University of Bayreuth (Göckede, 2001). Since flux footprint modeling can provide an accurate estimate of the shape, size, and orientation of the source area, we selected for turbulent sensible and latent heat fluxes of water tracks if the median contribution ≥ 79 % from water tracks pixels in the land cover map (Fig. 3). Since there was a good match between the size of flux source area and the surface area of the water track, this spatiotemporal filtering is expected to isolate the contribution of the water track to the SEB in the MDV in a meaningful fashion. The land cover matrix was generated by mapping the main land cover classes on a Quickbird satellite image. The used land cover classes include modern stream channels, wet water-track soils, paleolake delta sediments, glacial tills, and exposed ice. Pixel classification was done on the basis of albedo, texture, and field descriptions. Water tracks were mapped as multi-segment lines and were assigned a constant width of 10 m derived from the in-situ visual observations. Stream channels were mapped as multi-segment lines and were assigned a fixed width of 20 m. Landscape regions were given a single classification code avoiding any overlap. Features were mapped to provide continuous plan-view coverage with no gaps between features and no unassigned cells. Vector landscape features were rasterized at $10 \, \mathrm{m} \, \mathrm{px}^{-1}$ and were exported into a local Lambert Conformal Conic projection to produce gridded land use values. Each class was assigned an adequate momentum surface roughness length from literature.

5 Results and discussion

Differences in surface energy fluxes between the two reference stations were smaller than those between water-track and reference surfaces (see statistical analyses in Appendix B). We hence present the results by comparing average observations at the water track location against observations averaged over both reference locations. The recording period was sufficiently long to calculate meaningful average diurnal variations and daily totals of energy fluxes for both surfaces. Averaged over the entire observational period of 26 days, mean diurnal variations and daily totals of the SEB components showed that more than 50 % of the net radiation Q_S^* was transferred to sensible heat flux Q_H at both reference and water track, about 30 % to melting the permafrost (Q_{IT}), and the remainder to latent heat flux Q_{LE}. The net energy flux in the thawed layer (ΔS_{TL}) was zero and $Q_{IT} \approx Q_G$ (Fig. 4 and Fig. 5).
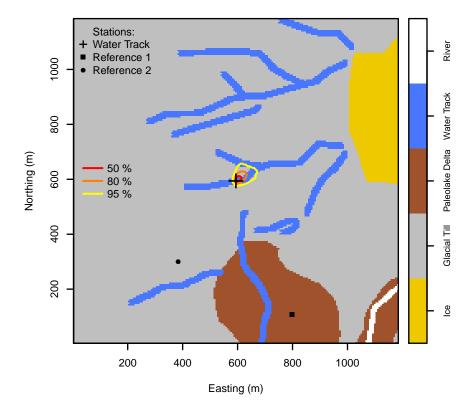
Figure 3. Excerpt of the land use matrix for lower Taylor Valley with Eddy-Covariance station locations. Water-track station with flux footprint including three density lines.

5.1 Net radiation

Magnitudes and average daily totals of Q_S^* were increased by a factor of 1.1 at the water track relative to the reference (Fig. 4 and Fig. 5) determined from a linear correlation. The increased Q_S^* values at the water track were in part caused by its lower albedo of 0.13 ± 0.01 when averaged over radiation measurements between 11:00 AM and 1:00 PM local time. In contrast, the reference mean albedo was 0.16 ± 0.01. In addition, the increased Q_S^* at the water track was can be explained by the reduced energy loss through upwelling longwave radiation due to lower surface temperatures compared to the reference surfaces. This reduced surface heating at the water track explains why the differences in Q_S^* between water-track and reference stations are greatest around solar noon when solar zenith angles are smallest (Fig. 6).

5.2 Turbulent heat fluxes

Average daily totals of the combined turbulent heat fluxes $Q_H + Q_{LE}$ reached 11 MJ at both the water track and the reference (Fig. 4). The partitioning between Q_H and Q_{LE}, however, strongly differed: At the water track magnitudes of Q_{LE} computed from linear correlation were increased by a factor of 3.0 relative to the reference, while magnitudes of Q_H were reduced down
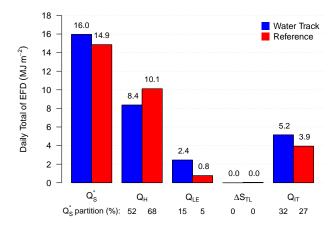
Figure 4. Ensemble mean daily totals of energy flux densities (EFD) of net radiation (Q_S^*), sensible heat flux (Q_H), latent heat flux (Q_{LE}), energy storage change in the thawed layer (ΔS_{TL}) and soil heat flux at ice table depth (Q_{IT}) for reference and water-track stations, averaged over whole measuring period. Partitions of Q_S^* at Water Track and Reference are added in % for each heat flux.

to 0.7 (Fig. 4). Daily heat flux totals at the water track were increased by a factor of 3.2 for Q_{LE} and reduced down to 0.8 for Q_H compared to the reference. Q_{LE} peaked earlier in the day while Q_H reached its maximum later at the water track compared to the reference. Turbulent heat fluxes reached their daily maximum in the afternoon irrespective of the surface (Fig. 6).

The increased water content of the water track-soil was likely the cause for increased Q_{LE} and reduced Q_H. The high
5 soil moisture also led to the earlier, longer and more pronounced daily peak of Q_{LE} at the water track. The resulting strong evaporative cooling restricted the surface energy exchange through Q_H by delaying surface warming at the water track. This finding is likely to serve as an explanation why Q_H showed a later and less distinct daily maximum compared to the reference, where energy is preferentially exchanged through Q_H. The maximum turbulence intensity was observed in the late afternoon hours, which led to the concurrent peak in turbulent fluxes.

10 ## 5.3 Conductive heat fluxes

Linear correlation of the conductive heat fluxes between water track and reference yielded an increase by a factor of 1.4 for Q_G and by 1.8 for ΔS_{TL} at the water track. Average diurnal variations of Q_{IT} showed a substantial scatter preventing a meaningful correlation. Average daily totals at the water track were increased by a factor of 1.3 for Q_G and Q_{IT} relative to the Reference while they were zero for ΔS_{TL} (Fig. 4 and Fig. 5). On average, Q_G was directed into the soil except at low solar
15 elevation angles between 09:30 PM and 3:30 AM, where the net energy transported was directed out of the soil to the surface. ΔS_{TL} changed sign approximately every 12 hours, turning the thawed layer from an energy sink into a source. Q_{IT} remained positive throughout the day when averaged over the entire observational period. The mean daily peak of Q_{IT} occurred earlier for the water track than for the Reference.(Fig. 6).

The distinctly higher Q_G and ΔS_{TL} at the water track compared to the reference at the time of the daily maximum can be
20 explained by the higher thermal conductivity of the water track-soil ($1.19 \pm 0.04 \ \mathrm{Wm^{-1}K^{-1}}$) compared to the reference 1
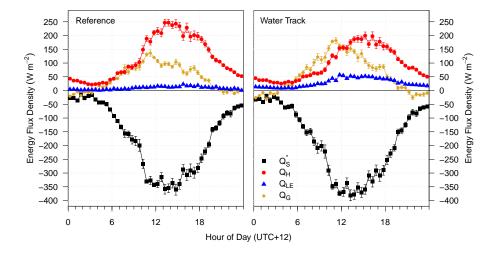
Figure 5. Ensemble mean diurnal variations of net radiation (Q_S^*), sensible heat flux (Q_H), latent heat flux (Q_{LE}) and ground heat flux (Q_G) for reference and water-track stations, averaged over the whole measuring period. Negative fluxes are directed to the ground surface, positive fluxes away from it. Error bars depict standard errors of the mean.

($0.39 \pm 0.17 \, \mathrm{Wm^{-1}K^{-1}}$). The simultaneous occurrence of negative Q_G and positive Q_{IT} at low solar elevation angles reveals a divergence of ΔS_{TL} which was directed both towards the surface and the ice table during these times. The increased water track Q_{IT} relative to the reference can be explained by the larger amount of ice in the frozen layer and the stronger transport of energy through the thermally more conductive thawed layer. The daily peaks of Q_{IT} are caused by the time-delayed daily peaks of Q_G from the previous day and the earlier peak of Q_{IT} at the water track relative to the reference. These findings suggest a faster transport of energy through the thawed layer due to its increased thermal conductivity.

5.4 Climate change scenarios

How will expected 21st century warming in the MDV impact mass and energy fluxes related to water tracks (Arblaster and Meehl, 2006; Chapman and Walsh, 2007)? To provide some answer based upon our evaluation of the SEB of water tracks, we briefly consider three possible scenarios: One where water track spatial extent increases due to increased melting of surface snow (Gooseff et al., 2013; Langford et al., 2015; Levy, 2015), one where insolation increases but regional air temperatures remain constant (Gooseff et al., 2017), and one where temperatures increase but insolation remains constant, which corresponds to a more typical Arctic-type climatology. This discussion is meant to frame possible energy and mass flux scenarios for the MDV based on the measurements made in this study informed by meteorological first principles, and could serve as a basis for advanced micro-scale modeling to provide constraints on the timing and spatial feedbacks of these predicted mechanisms.

We estimated the average daily evaporation E spatially integrated for the entire lower Taylor Valley using the abundance of water tracks in the land use matrix. The daily E of $1.00 \, \mathrm{mm \, d^{-1}}$ measured for the water track was assigned to all water track-cells, while the total E of $0.27 \, \mathrm{mm \, d^{-1}}$ measured for reference was assigned to all remaining non-water track cells. The

The Cryosphere
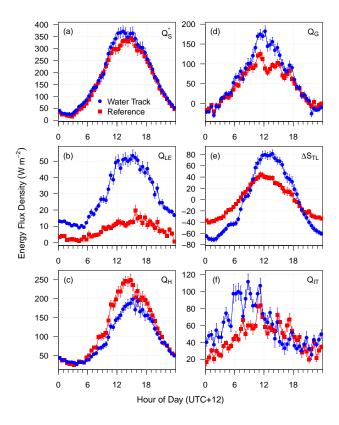Discussions

Figure 6. Comparison of diurnal variations of net radiation Q_S^* (**a**), latent heat flux Q_{LE} (**b**), sensible heat flux Q_H (**c**), ground heat flux Q_G (**d**), energy storage change in the thawed layer ΔS_{TL} (**e**) and soil heat flux at ice table depth Q_{IT} (**f**) between water-track (blue circles) and reference (red squares) locations, averaged over the entire measuring period of 26 days. Negative energy fluxes are directed into the ground surface, while positive fluxes point away from it. However, for ΔS_{TL} positive fluxes are directed into the thawed layer and negative fluxes out of the thawed layer. Error bars depict standard errors of the mean.

fraction of bare soil in the matrix occupied by water tracks was 2.9 %. The resulting mean E from the entire lower Taylor Valley in its current composition was determined as 0.29 $\mathrm{mm\,d^{-1}}$.

In our first scenario, we simply assumed an increase of the relative water track fraction by 50% by increased snow melt, which results in a total of 4.4 %: This change would lead to an increase in E from the entire lower Taylor Valley by 4 % to 0.30 $\mathrm{mm\,d^{-1}}$. Now we consider the remaining two alternate scenarios, for which we cannot make any quantitative estimates but only offer mechanistic predictions: In the scenario of constant insolation and rising temperatures in the MDV, an increase in vapor pressure deficit would lead to delayed cloud formation and precipitation while net radiation would increase because of reduced cloud coverage, causing a positive feedback on temperature. The increased temperature would act to intensify snowmelt and thus increase the water track-coverage. If temperatures stay constant and insolation increases as observed by Gooseff et al. (2017), higher net radiation will cause an evaporation increase which will reduce the vapor pressure deficit

since air temperatures remain constant. The increased cloud formation would then cause a negative feedback on insolation and weaken the increase in water track-coverage.

6 Conclusions

In this study, we aimed at characterizing the energy exchange across contrasting surfaces of water tracks and non-water tracks composed of glacial till and paleolake delta sediments in lower Taylor Valley, McMurdo Dry Valleys, Antarctica. The findings support our initial hypothesis that water tracks significantly modify the surface energy budget of the terrestrial Antarctic due to lowered surface albedo and increased water content in the active layer, leading to an enhanced cycling of energy and mass.

Water Track shows an increase in net radiation, latent heat flux, and soil heat flux in the thawed and frozen layers, as well as a decreased sensible heat flux relative to the reference data. For both the water track and reference locations, the sensible heat flux was observed to be the largest component consuming ≈ 50 % of the net radiation. The second largest energy sink was the soil heat flux at ice table depth, which provides the heat for the lowering of the ice table by melting, being ≈ 30 % of the net radiation. Its magnitude was larger than that of the latent heat flux, i.e., evaporation. Considering a realistic scenario of an increase in abundance of water tracks with the observed properties in lower Taylor Valley would cause a noticeable enhancement in evaporation from this Antarctic landscape.

In summary, our findings provide convincing evidence that water tracks in the McMurdo Dry Valleys have a strong impact on the surface energy balance, particularly on the latent heat flux, by increasing the uptake of energy at the surface. This leads us to conclude that water tracks will respond faster to the changing climate in the McMurdo Dry Valleys than any other dry soil surfaces, which are more abundant. The magnitude and rate of this response will depend on the exact mechanism forcing the change by ither changes in temperature or insolation.

Data availability. The data analyzed in this study are in the process of being published on the PANGAEA Data Publisher.

Appendix A: Sensitivity of energy storage change in the thawed layer to ice table depth

Since only one measurement for the ice table depth z_{IT} of each station was taken, an analysis of the sensitivity of ΔS_{TL} to a variation of z_{IT} was appropriate because we assumed that the thawed layer was spatially heterogeneous and a temporal increase in z_{IT} owing to the thawing process was taking place. To analyze this sensitivity, we compared ΔS_{TL} calculated using measured $z_{IT} = 0.48$ m at the Water Track and $z_{IT} = 0.30$ m at the Reference with alternative ΔS_{TL} resulting from assuming $z_{IT} = 0.30$ m at the Water Track and $z_{IT} = 0.48$ m at the Reference. This comparison was done with root mean-squared errors (RMSE):

$$\text{RMSE} = \sqrt{\frac{1}{48} \sum_{i=1}^{48} (x_1 - x_2)^2}, \tag{A1}$$

Table A1. Using root mean-squared errors (RMSE) calculated with Eq. (A1) for the comparison of mean diurnal variations of energy storage change in the thawed layer (ΔS_{TL}) over the whole measuring period between parameters x_1 vs. x_2. **(a)** Comparison between water-track (WT) and reference (Ref) values with measured ice table depths (z_{IT}). **(b)** Sensitivity of ΔS_{TL} to different z_{IT} values at the Water Track, where measured z_{IT} is assigned to x_2. **(c)** Same as **(b)**, but for reference data.

	(a) WT vs. Ref	**(b) WT Sensitivity**	**(c) Ref Sensitivity**
x_1	$\Delta S_{TL,WT}(z_{IT} = 0.48\,m)$	$\Delta S_{TL,WT}(z_{IT} = 0.30\,m)$	$\Delta S_{TL,Ref}(z_{IT} = 0.48\,m)$
x_2	$\Delta S_{TL,Ref}(z_{IT} = 0.30\,m)$	$\Delta S_{TL,WT}(z_{IT} = 0.48\,m)$	$\Delta S_{TL,Ref}(z_{IT} = 0.30\,m)$
RMSE ($Wm^{-}2$)	27.62	7.18	3.90

where i runs from 1 to 48 to include all half-hour values of the mean diurnal variations and x_1 and x_2 correspond to ΔS_{TL} values specified for three cases (Table A1): (a): ΔS_{TL} with measured z_{IT} was compared between Water Track and Reference. (b) and (c): RMSE between ΔS_{TL} computed using measured vs. alternative z_{IT} was determined for Water Track and Reference, respectively, quantifying the sensitivity of ΔS_{TL} to uncertainty of z_{IT} for both Water Track and Reference. RMSE between
5 Water Track and Reference was around 4 and 7 times as high as the RMSE sensitivity estimates for Water Track and Reference, respectively (Table A1), which provides evidence that sensitivity of ΔS_{TL} to uncertainty of z_{IT} is negligible compared to the impact of the Water Track on ΔS_{TL} relative to the Reference.

Appendix B: Influence of different reference surfaces on surface energy balance

Reference 1 was located in a paleolake delta and was characterized by fine material while the glacial till at Reference 2 had a
10 coarse texture. Differences in texture and other properties of the surfaces, e.g. albedo, may lead to considerable differences in surface energy fluxes between the two reference surfaces. These disparities between the reference stations were compared to differences between Water Track and Reference via two statistical estimates, RMSE1 and RMSE2, to examine if the influence of the Water Track on the SEB is more significant than the effect of other surface properties.

RMSE1 represents the differences between water-track and reference energy fluxes and is calculated as the root mean-
15 squared error (RMSE) of mean diurnal variations of energy fluxes at the Water Track relative to reference values:

$$\text{RMSE1}_x(t_j) = \sqrt{\frac{1}{48}\sum_{i=1}^{48}\left(Q_{x,WT,i}(t_j) - Q_{x,Ref,i}(t_j)\right)^2}, \tag{B1}$$

where x specifies the SEB component and t_j stands for the periods t_1 and t_2 representing the recording periods of Reference 1 and Reference 2, respectively. RMSE2 compares the differences between surface energy fluxes of water-track and reference stations at t_1 to those at t_2:

20 $$\text{RMSE2}_x = \sqrt{\frac{1}{48}\sum_{i=1}^{48}\left[(Q_{x,WT,i}(t_1) - Q_{x,Ref,i}(t_1)) - (Q_{x,WT,i}(t_2) - Q_{x,Ref,i}(t_2))\right]^2}. \tag{B2}$$
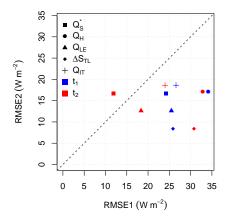
Figure B1. Investigating differences between surface energy fluxes at Reference 1 and Reference 2 via comparison of two statistical estimates using mean diurnal variations and based on root mean-squared errors (RMSE): RMSE1 quantifies differences between water-track and reference values separately for recording periods of Reference 1 (t_1) and of Reference 2 (t_2). RMSE2 calculates the change from t_1 to t_2 of differences between water-track and reference values which represents the disparity of the reference surfaces, cleared of the influence of meteorological boundary conditions. Computation of RMSE1 and RMSE2 for net radiation (Q_S^*), sensible heat flux (Q_H), latent heat flux (Q_{LE}), heat storage change in the thawed layer (ΔS_{TL}) and soil heat flux at ice table depth (Q_{IT}).

Thus, RMSE2 represents the disparity of the two reference surfaces, compensating for temporal changes of absolute energy flux values caused by varying meteorological conditions between t_1 and t_2.

For most SEB components, $\text{RMSE1}_x(t_j)$ was larger than RMSE2_x. Only for Q_S^*, $\text{RMSE1}_{Q_S^*}(t_2)$ was smaller than $\text{RMSE2}_{Q_S^*}$ (Fig. B1). This indicates that for most SEB components and both reference stations, the differences between water-track and reference surfaces were larger than between the two reference surfaces, except for Q_S^* at Reference 2. Hence, the impact of water tracks on surface energy fluxes was generally more important than the effect of soil texture and other properties varying between Reference 1 and Reference 2. For Q_S^*, differences between Reference 2 and Water Track were less significant than the difference between Reference 1 and Reference 2, which can be explained by very similar albedo at Reference 2 and Water Track.

Appendix C: Soil thermometers

Author contributions. CT designed the experiment. JL and CT carried it out, where JL focused on soil measurements and CT was responsible for Eddy-Covariance and radiation measurements. TL performed the footprint simulations and analyzed the results, with support from CT. TL prepared the manuscript with contributions from all co-authors.

The Cryosphere
Discussions

Open Access

EGU

Table C1. Soil thermometer devices, depths of their deployment and recording periods for all three stations.

Station	TC Depths (cm)	TC Recording Periods	TR Depths (cm)	TR Recording Periods
Water Track	0.4	26 December 2012–04 January 2013	1,4,12,22	04 January 2013–21 January 2013
	0.4	26 December 2012–21 January 2013		
Reference 1	0.4,0.4	27 December 2012–04 January 2013	4,7,30	28 December 2012–14 January 2013
	1,4,12	04 January 2013–14 January 2013		
Reference 2	1,4,12	14 January 2013–21 January 2013	-	-

TC: Thermocouples (*TMTSS-020, OMEGA Engineering Inc., Norwalk, CT, USA*).

TR: Thermistors, recorded with *HOBO H8 Pro* logger from *Onset Computer Corp., Bourne, MA, USA*.

Competing interests. The authors declare that they have no conflict of interest.

References
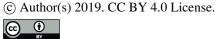
Arblaster, J. M. and Meehl, G. A.: Contributions of External Forcings to Southern Annular Mode Trends, Journal of Climate, 19, 2896–2905, https://doi.org/10.1175/JCLI3774.1, 2006.

5 Aubinet, M., Grelle, A., Ibrom, A., Rannik, U., Moncrieff, J., Foken, T., Kowalski, A. S., Martin, P. H., Berbigier, P., Bernhofer, C., Clement, R., Elbers, J., Granier, A., Grunwald, T., Morgenstern, K., Pilegaard, K., Rebmann, C., Snijders, W., Valentini, R., and Vesala, T.: Estimates of the annual net carbon and water exchange of forests: The EUROFLUX methodology, Advances in Ecological Research, Vol 30, 30, 113–175, 2000.

Baldocchi, D. D.: Assessing the eddy covariance technique for evaluating carbon dioxide exchange rates of ecosystems: past, present and future, Global Change Biol., 9, 479–492, 2003.

10 Ball, B. A. and Levy, J.: The role of water tracks in altering biotic and abiotic soil properties and processes in a polar desert in Antarctica, Journal of Geophysical Research: Biogeosciences, 120, 270–279, https://doi.org/10.1002/2014JG002856, 2015.

Chapman, W. L. and Walsh, J. E.: A Synthesis of Antarctic Temperatures, Journal of Climate, 20, 4096–4117, https://doi.org/10.1175/JCLI4236.1, 2007.

Christensen, J. H., K. Krishna Kumar, E. Aldrian, S.-I. An, I.F.A. Cavalcanti, M. de Castro, W. Dong, P. Goswami, A. Hall, J.K. Kanyanga,
15 A. Kitoh, and J. Kossin: Climate Phenomena and their Relevance for Future Regional Climate Change, in: Climate change 2013, edited by Stocker, T. F., D. Qin, G.-K. Plattner, M. Tignor, S.K. Allen, J. Boschung, A. Nauels, Y. Xia, V. Bex, and P.M. Midgley, pp. 1217–1308, Cambridge University Press, Cambridge, https://doi.org/10.1017/CBO9781107415324.028, 2014.

Doran, P. T., Priscu, J. C., Lyons, W. B., Walsh, J. E., Fountain, A. G., McKnight, D. M., Moorhead, D. L., Virginia, R. A., Wall, D. H., Clow, G. D., Fritsen, C. H., McKay, C. P., and Parsons, A. N.: Antarctic climate cooling and terrestrial ecosystem response, Nature, 415,
20 517–520, https://doi.org/10.1038/nature710, 2002b.

Foken, T., Göckede, M., Mauder, M., Mahrt, L., Amiro, B., and Munger, W.: Post-Field Data Quality Control, in: Handbook of Micrometeorology, edited by Lee, X., Law, B., and Massman, W., Atmospheric and Oceanographic Sciences Library, pp. 181–208, Springer Science + Business Media Inc, Dordrecht, 2004.

Fountain, A. G., Fernandez-Diaz, J. C., Obryk, M., Levy, J., Gooseff, M., van Horn, D. J., Morin, P., and Shrestha, R.: High-resolution
25 elevation mapping of the McMurdo Dry Valleys, Antarctica, and surrounding regions, Earth System Science Data, 9, 435–443, https://doi.org/10.5194/essd-9-435-2017, 2017.

Göckede, M.: Die Verwendung des footprint-Modells nach SCHMID (1997) zur stabilitätsabhängigen Bestimmung der Rauhigkeitslänge, Arbeitsergebnisse, Universität Bayreuth, Abt. Mikrometeorologie, https://epub.uni-bayreuth.de/267/, 2001.

Gooseff, M. N., Barrett, J. E., and Levy, J. S.: Shallow groundwater systems in a polar desert, McMurdo Dry Valleys, Antarctica, Hydroge-
30 ology Journal, 21, 171–183, https://doi.org/10.1007/s10040-012-0926-3, 2013.

Gooseff, M. N., Barrett, J. E., Adams, B. J., Doran, P. T., Fountain, A. G., Lyons, W. B., McKnight, D. M., Priscu, J. C., Sokol, E. R., Takacs-Vesbach, C., Vandegehuchte, M. L., Virginia, R. A., and Wall, D. H.: Decadal ecosystem response to an anomalous melt season in a polar desert in Antarctica, Nature ecology & evolution, 1, 1334–1338, https://doi.org/10.1038/s41559-017-0253-0, 2017.

Ikard, S. J., Gooseff, M. N., Barrett, J. E., and Takacs-Vesbach, C.: Thermal characterisation of active layer across a soil moisture gradient
35 in the McMurdo Dry Valleys, Antarctica, Permafrost and Periglacial Processes, 20, 27–39, https://doi.org/10.1002/ppp.634, 2009.

Langford, Z. L., Gooseff, M. N., and Lampkin, D. J.: Spatiotemporal dynamics of wetted soils across a polar desert landscape, ANTARCTIC SCIENCE, 27, 197–209, https://doi.org/10.1017/S0954102014000601, 2015.

Leclerc, M. and Foken, T.: Footprints in micrometeorology and mcology, Springer-Verlag, Heidelberg, 2014.

Levy, J.: How big are the McMurdo Dry Valleys? Estimating ice-free area using Landsat image data, Antarctic Science, 25, 119–120, https://doi.org/10.1017/S0954102012000727, 2013.

Levy, J.: A hydrological continuum in permafrost environments: The morphological signatures of melt-driven hydrology on Earth and Mars, GEOMORPHOLOGY, 240, 70–82, https://doi.org/10.1016/j.geomorph.2014.02.033, 2015.

Levy, J. S. and Schmidt, L. M.: Thermal properties of Antarctic soils: Wetting controls subsurface thermal state, Antarctic Science, 28, 361–370, https://doi.org/10.1017/S0954102016000201, 2016.

Levy, J. S., Fountain, A. G., Gooseff, M. N., Welch, K. A., and Lyons, W. B.: Water tracks and permafrost in Taylor Valley, Antarctica: Extensive and shallow groundwater connectivity in a cold desert ecosystem, Geological Society of America Bulletin, 123, 2295–2311, https://doi.org/10.1130/B30436.1, 2011.

Liebethal, C. and Foken, T.: Evaluation of six parameterization approaches for the ground heat flux, Theoretical and Applied Climatology, 88, 43–56, https://doi.org/10.1007/s00704-005-0234-0, 2007.

Lloyd, C. R., Harding, R. J., Friborg, T., and Aurela, M.: Surface fluxes of heat and water vapour from sites in the European Arctic, Theoretical and Applied Climatology, 70, 19–33, https://doi.org/10.1007/s007040170003, 2001.

Lyons, W. B., Andrew G. Fountain, Peter T. Doran, John C. Priscu, Klaus Neumann, and Kathleen A. Welch: Importance of landscape position and legacy: The evolution of the lakes in Taylor Valley, Antarctica, Freshwater Biology, 43, 355–367, https://doi.org/10.1046/j.1365-2427.2000.00513.x, 2000.

Moore, C. J.: Frequency response corrections for eddy correlation systems, Boundary-Layer Meteorology, 37, 17–35, https://doi.org/10.1007/BF00122754, 1986.

Pachauri, R. K. and Mayer, L., eds.: IPCC, 2014: Climate Change 2014: Synthesis Report: Contribution of Working Groups I, II and III to the Fifth Assessment Report of the Intergovernmental Panel on Climate Change, Intergovernmental Panel on Climate Change, Geneva, Switzerland, 2015.

Schotanus, P., Nieuwstadt, F., and de Bruin, H.: Temperature measurement with a sonic anemometer and its application to heat and moisture fluxes, Boundary-Layer Meteorology, 26, 81–93, https://doi.org/10.1007/BF00164332, 1983.

Thomas, C. K., Law, B. E., Irvine, J., Martin, J. G., Pettijohn, J. C., and Davis, K. J.: Seasonal hydrology explains interannual and seasonal variation in carbon and water exchange in a semiarid mature ponderosa pine forest in central Oregon, Journal of Geophysical Research, 114, 714, https://doi.org/10.1029/2009JG001010, 2009.

Vickers, D. and Mahrt, L.: Quality Control and Flux Sampling Problems for Tower and Aircraft Data, Journal of Atmospheric and Oceanic Technology, 14, 512–526, https://doi.org/10.1175/1520-0426(1997)014<0512:QCAFSP>2.0.CO;2, 1997.

Webb, E. K., Pearman, G. I., and Leuning, R.: Correction of flux measurements for density effects due to heat and water vapour transfer, Quarterly Journal of the Royal Meteorological Society, 106, 85–100, https://doi.org/10.1002/qj.49710644707, 1980.

Wilczak, J. M., Oncley, S. P., and Stage, S. A.: Sonic Anemometer Tilt Correction Algorithms, Boundary-Layer Meteorology, 99, 127–150, https://doi.org/10.1023/A:1018966204465, 2001.